Materials Advances

ROYAL SOCIETY OF CHEMISTRY

PAPER

View Article Online
View Journal | View Issue

Cite this: *Mater. Adv.*, 2025, 6, 4833

Systematic study of CVD-growth parameters in NaCl-assisted growth of $MoSe_2$ nanostructures: nanoribbons, dendrites and spirals†

Mahima Tyagi, *[a] Srijata Dey,[a] Pinky Sahoo[b] and Deshdeep Sahdev[b]

$MoSe_2$, a two-dimensional (2D) transition metal dichalcogenide (TMDC), has garnered significant interest in recent years due to its semiconducting properties and tunable band gap with potential applications in optoelectronics, photocatalysis and atomically thin devices. In this study, we report the controlled synthesis of $MoSe_2$ nanocrystals using a custom 12-zone atmospheric pressure chemical vapour deposition (APCVD) system. NaCl is used as a seed promoter to facilitate the growth of monolayer, bilayer, and multilayer films, often as large as 200 μm. Additionally, the morphological evolution of the $MoSe_2$ nanostructures is controlled by tuning different growth parameters based on insights, which we discuss in detail. The growth of dominant nanostructures, which include nanoribbons, snowflakes, monolayers and multilayer domains, among others, are discussed. High-resolution optical microscopy, field emission scanning electron microscopy (FESEM) and atomic force microscopy (AFM) are used to image the as-grown crystals. Raman spectroscopy and X-ray photoelectron spectroscopy (XPS) are used to verify the quality and elemental composition of our as-grown $MoSe_2$ crystals. Our findings brighten the prospect of growing novel 1D and 2D TMDC nanostructures with sufficient control to make them suitable for advanced optoelectronic and catalytic devices.

Received 10th February 2025,
Accepted 31st May 2025

DOI: 10.1039/d5ma00121h

rsc.li/materials-advances

1. Introduction

Over the last decade, two-dimensional layered transition metal dichalcogenides (TMDCs), in general, have attracted significant attention because of their exceptional electronic and optical characteristics.[1–4] Of these, MoS_2 and $MoSe_2$ have been particularly popular because of the promise they hold for a range of applications. Within these, monolayer or few-layer $MoSe_2$ nanostructures exhibit superior behaviour to MoS_2 due to their unique band structures.[5–8] Few-layer 2D TMDCs, including $MoSe_2$, offer enhanced mechanical and chemical stability compared to their monolayer counterparts, making them more suitable for use in FETs. This stability is crucial, as it allows these materials to withstand the harsh conditions encountered during device fabrication. An increased number of layers also provides a larger number of transport channels and results in higher on-state current and carrier mobility.[9]

Chemical vapor deposition (CVD) has been widely used to synthesize highly crystalline and large-area $MoSe_2$ films. The successful growth of $MoSe_2$ on SiO_2/Si substrates using CVD was first reported by Shaw *et al.*[10] Since then, there have been several reports of large-area $MoSe_2$ nanocrystals grown by CVD on many other substrates.[11–14] Chang *et al.*[7] compared the optical and electronic properties of CVD-grown MoS_2 and $MoSe_2$ and found that the number of defects was lower in the latter. This was in part explained by Wang *et al.*,[15] who initiated a discussion of the growth mechanisms involved in CVD-grown $MoSe_2$.

Two of the important growth mechanisms are worth noting. With the metal oxide precursor and substrate conventionally placed in a high-temperature zone, and the chalcogen in a relatively low-temperature region[12] crystals grow in the vapor–solid–solid (VSS) mode, wherein a solid crystal is deposited directly from the vapor phase onto a solid substrate. Vapor phase precursors directly adsorb and react on the substrate surface to form nuclei, which subsequently grow into solid, typically triangular or hexagonal, domains. These shapes are dictated primarily by the free energy of the crystal edges and the surface diffusion kinetics of the precursors. However, the morphologies produced by this route are limited.

In contrast, the vapor–liquid–solid (VLS) mode, facilitated by the introduction of alkali halide salts, *e.g.* NaCl or KCl, alters the free energy of the crystal edges[16,17] and opens out several

[a] *Department of Physics, Birla Institute of Technology and Science, Pilani, Pilani Campus, Vidya Vihar, Pilani, Rajasthan 333031, India. E-mail: mahima01tg@gmail.com*
[b] *Research Division, Quazar Technologies, Sarvapriya Vihar, New Delhi 110016, India*

† Electronic supplementary information (ESI) available. See DOI: https://doi.org/10.1039/d5ma00121h

new possibilities. This mechanism involves vapor-phase precursors adsorbing onto a catalytic liquid metal droplet, dissolving therein, and later precipitating at the liquid–solid interface to produce a range of nanostructures such as nanowires and nanoribbons. Several van der Waals layered compounds, including BN,[18] $NiCl_2$,[19] SnS_2[20] and Bi_2Se_2,[21] have been synthesized by this method. However, control of the morphology and quality of the resulting $MoSe_2$ nanostructures continues to be an outstanding challenge.

In this context, it is worth mentioning that the addition of alkali halides to the metal oxide enhances the growth rates and sizes of the resulting crystals (or continuous films) and reduces the growth temperature. Li *et al.*[22] reported that large WSe_2 and WS_2 monolayer crystals could be grown at moderate temperatures (700–850 °C) using alkali metal halides as growth promoters. Li *et al.*[23] demonstrated a dramatic enhancement in the growth of 2D TMDC selenides and tellurides, namely $MoSe_2$ and WTe_2, using mixed transition metal salts and chalcogen salts. The addition of salts induced the wafer-scale growth of these TMDCs, forming a continuous monolayer film and a large gain size of 100–50 μm. Kim *et al.*[24] made the same observation with regard to MoS_2. Zhou *et al.*[25] subsequently demonstrated that molten-salt-assisted CVD can be broadly applied to produce atomically thin TMDC films. They also showed that salt assistance increases the overall reaction rate by decreasing the melting point of the reactants, which in turn facilitates the formation of intermediate products. For example, metaloxyhalides, formed in reactions between halides and metal oxides, evaporate at relatively low temperatures, enhancing 2D growth in the process. Chen *et al.*[5] reported the controlled CVD growth of large-scale monolayer and multi-layer $MoSe_2$ films and nanoribbons. Li *et al.*[26] synthesised single-crystal, monolayer $MoSe_2$, with domain sizes reaching up to 250 μm, by employing NaCl-assisted CVD. Feng *et al.*[27] reported that increasing the growth temperature in the presence of NaCl leads to drastic changes in the morphology of the as-grown WSe_2 samples. Singh *et al.*[28] similarly grew MoS_2 on different substrates and demonstrated that NaCl facilitates the formation of seeding promoters, such as a water-soluble layer of Na_2S and/or Na_2SO_4 on the substrate, which aids in the 2D planar nucleation of MoS_2. Bay *et al.*[29] further systematised this approach by growing $MoSe_2$ nanocrystals, using five different water-soluble catalysts, namely sodium chloride (NaCl), zinc chloride ($ZnCl_2$), potassium hydroxide (KOH), potassium chloride (KCl), and potassium oxalate ($K_2C_2O_4$). These were applied as thin layers onto the SiO_2/Si substrates. Among these five salts, the use of NaCl resulted in the most uniform growth of the as-synthesised flakes.

Each TMDC morphology, including nanoribbons, dendrites, fractals, and spiral formations, offers distinct advantages for various applications. For example, 1D nanoribbons have shown significant promise in electronic, magnetic, and catalytic applications;[30–33] however, the controllable fabrication of $MoSe_2$ nanoribbons is found to be scant in the literature. Similarly, dendritic and fractal structures are particularly advantageous for catalytic applications owing to the high density of the active edge sites and defects they possess. Studies have shown that the rate of the hydrogen evolution reaction (HER) increases linearly with the density of these features.[34–37] The CVD growth of MoS_2 dendrites, as reported earlier by our group,[38] can be further enhanced by adding NaCl to the precursor. The formation of dendrites or fractals in $MoSe_2$ under optimised CVD-growth conditions, as reported here, would be suitable for HER catalytic activity. Additionally, spiral structures, which interlink the layers of $MoSe_2$, provide unique pathways for electrical current, enhancing the vertical conductivity of the devices. This unique morphology was found to notably increase the vertical conductivity in MoS_2,[39] enhancing the overall electrical conductivity and making these structures ideal for use in nanoelectronic devices.[40] Moreover, the non-inversion symmetry present in these nanostructures gives rise to interesting nonlinear optical (NLO) effects, polarization and piezoelectricity, all of which promise to find applications in electronics and optoelectronics.[41–43]

In this study, we systematically investigate the morphological evolution of $MoSe_2$ nanocrystals by varying a set of specific CVD-growth parameters. NaCl is employed as a seed promoter to enhance both the growth rate and size of the crystals. By meticulously tuning these parameters, a wide variety of nanocrystal morphologies were successfully synthesized. There are several studies on NaCl-assisted CVD growth of TMDCs available in the literature, as mentioned earlier; but in addition, there are substantial research gaps. Our studies are an attempt to address this gap by correlating the CVD growth of each of these different $MoSe_2$ nanostructures, including nanoribbons, dendrites, and spiral structures, with specific regions of parameter space. This is essential for the controlled growth of large-area crystals with desired morphologies. Initially, an optimal NaCl concentration was identified to facilitate the formation of large flakes. Under these conditions, nanoribbons emerged as the predominant nanostructure. Subsequently, by varying the growth temperature and the concentration of the chalcogen precursor, a diverse array of nanostructures was obtained. This comprehensive analysis defines the range of achievable morphologies and offers valuable insights into the underlying growth mechanisms driving their formation.

2. Experimental details

Fig. 1(a) depicts a schematic diagram of the (CVD) setup for $MoSe_2$ growth. The CVD experiments were carried out in a commercial APCVD system, QRYSTAL-CVD-1100,[44] manufactured by Quazar Technologies.[45] The furnace comprises twelve independent, 75 mm-long thermal zones, each equipped with its own heater and temperature sensor. The temperature of each zone is individually adjustable through an intuitive graphical user interface, allowing for seamless control. Adjacent zones can be integrated by synchronizing their set temperatures, enabling the formation of composite heating regions of variable lengths. These zones maintain a temperature uniformity of ±5 °C. This sophisticated system facilitates exceptional control over growth parameters, ensuring the high precision necessary for the demands of this study.

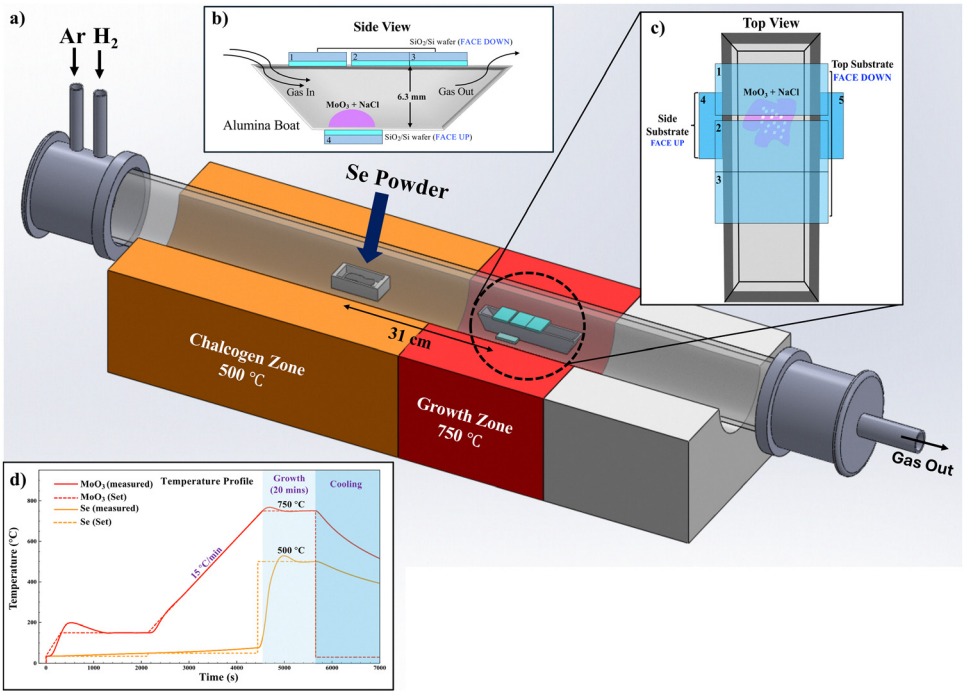

Fig. 1 (a) Schematic illustration showing the experimental set-up for CVD of $MoSe_2$; (b) and (c) the side view and the top view of the substrates placed on the alumina boat containing MoO_3 and NaCl, respectively; (d) the temperature profile for the APCVD growth of $MoSe_2$.

For the deposition of $MoSe_2$, high-purity molybdenum trioxide (MoO_3, ≥99.5%, Sigma Aldrich), selenium (Se, ≥99.5%, Sigma Aldrich), and sodium chloride (NaCl) powders (99.9%, CDH) were used as precursors, and 300 nm thermally oxidised SiO_2/Si wafers were used as substrates. An alumina boat containing 1 mg of MoO_3 and three substrates placed face down on top of it (labelled 1, 2 and 3 in Fig. 1(c)) were loaded into the quartz tube. A gap of 0.5 mm was kept between wafers 1 and 2, which acts as an outlet for the precursor vapor. This ensures that some of the vapors escape the alumina boat, and uniform deposition on wafers 4 and 5 occurs, which were placed face-up adjacent to the alumina boat (Fig. 1(c)). The boat containing Se powder (600 mg) was placed upstream at a distance of 31 cm away from the MoO_3 boat (Fig. 1(a)). For the NaCl-assisted growth experiments, a mixture of the MoO_3 and NaCl powder was used.

Prior to deposition, the substrates (10 mm × 10 mm) were cleaned ultrasonically in acetone and isopropyl alcohol (IPA), respectively, and then dried under Ar gas. The alumina boat containing the mixture of MoO_3 and NaCl and the substrates was then loaded into a quartz tube. The CVD furnace was configured into two heating zones: a chalcogen zone heated up to 500 °C for Se vaporisation and the growth zone comprising MoO_3, NaCl and the substrates, which was heated up to a higher temperature for $MoSe_2$ synthesis. The temperature profile of these zones is shown in Fig. 1(b). The CVD system was initially evacuated and purged. This procedure was repeated five times over a total period of 30 minutes, during which the chalcogen zone and the growth zone were maintained at room temperature and 150 °C, respectively. Subsequently, the gas flow rate was set to 10 sccm, which comprised Ar (8 sccm) and H_2 (2 sccm), with H_2 acting as a reducing agent. The growth zone temperature was then ramped up at a rate of 15 °C min^{-1} until it reached 750 °C. Se was rapidly evaporated at 500 °C when the growth zone reached 725 °C. The system was maintained under this condition for 20 minutes. Finally, the system was cooled gradually with Ar flow at 200 sccm, stopping the H_2 flow.

2.1. Characterization

High-resolution optical images of the as-grown $MoSe_2$ flakes were captured using a Carl Zeiss Axio Lab. A1 microscope equipped with an AxioCam ERc5s camera. Raman spectra were recorded with a Horiba Jobin Yvon LabRAM HR spectrometer using a 532 nm excitation laser. X-ray photoelectron spectroscopy (XPS) measurements were conducted using a Thermo Fisher Scientific K-Alpha instrument. Field emission scanning electron microscopy (FESEM) images were acquired with an FEI Apreo LoVac microscope. Atomic force microscopy (AFM) measurements were performed using an Agilent LS5600 system.

3. Results and discussion

$MoSe_2$ crystals deposited using the standard recipe (without any NaCl) are triangular, with a maximum domain size of ~25 μm as shown in Fig. 2(a). The crystals grown are uniform monolayers, as confirmed by Raman spectra (Fig. 2(b)) obtained at different points on the same crystal. The standard A_{1g} (out-of-plane vibrational mode) and E_{2g} (in-plane vibrational mode) peaks for monolayer $MoSe_2$ are observed at 239.7 cm^{-1} and 286.2 cm^{-1}, respectively.[46] The combination

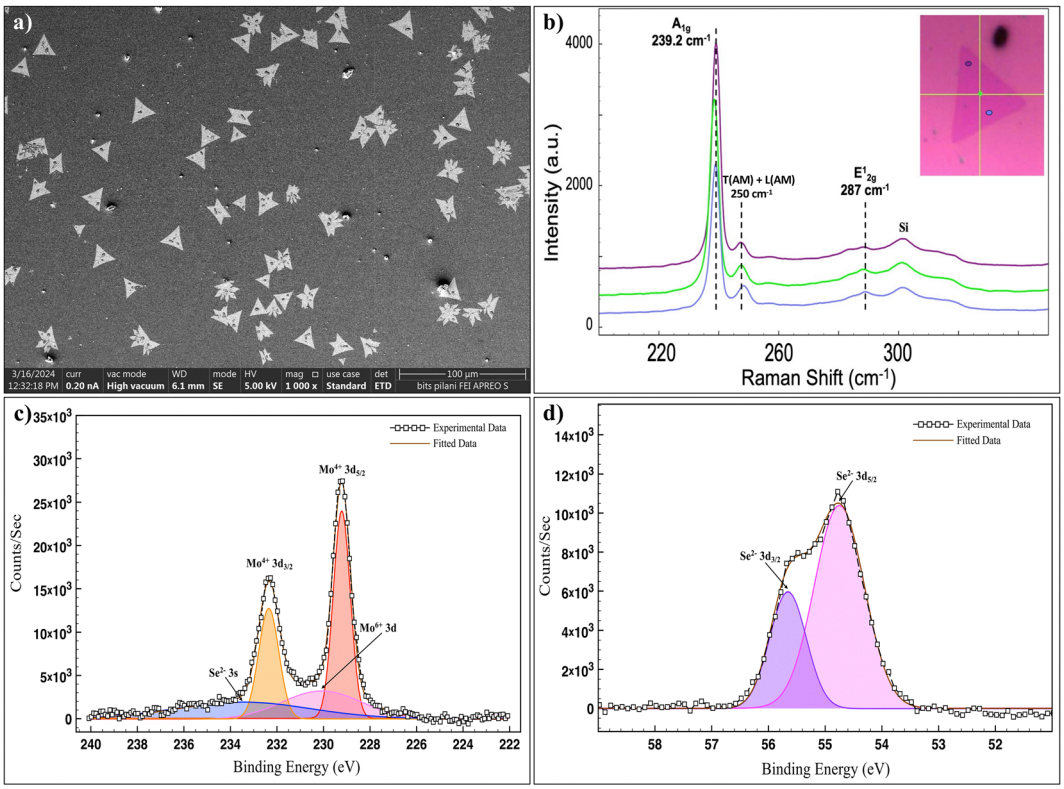

Fig. 2 (a) FESEM image of the as-grown $MoSe_2$ crystal on the SiO_2/Si substrate using the standard recipe (without NaCl) at a growth temperature of 750 °C. (b) Raman spectrum of $MoSe_2$. High-resolution deconvoluted XPS spectra of (c) Mo 3d and (d) Se 3d.

modes of the longitudinal (LA(M)) and the transverse (TA(M)), originating from the vicinity of the high-symmetry M point of the $MoSe_2$ Brillouin zone, are observed at 247.4 cm^{-1}.[47,48] Fig. 2(c) and (d) show high-resolution deconvoluted XPS spectra of Mo 3d and Se 3d core-level signals, respectively. The Mo $3d_{3/2}$ and $3d_{5/2}$ peaks are located at 232.5 eV and 229.3 eV, respectively, as depicted in Fig. 2(c). Those of Se are detected around 54 eV, as shown in Fig. 2(d). These data are in agreement with the respective values of $MoSe_2$ found in the literature.[14,49] These two Mo 3d peaks represent the oxidation charge state of $MoSe_2$. The Mo peak positions are shifted significantly from their hexavalent positions of ~235.9 eV and 232.5 eV (Mo $3d_{3/2}$ and $3d_{5/2}$ core levels of MoO_3), indicating the reduction of Mo from Mo 6p to Mo 4p. The two comparatively weak peaks present in the Mo 3d plot are linked to Mo^{6+} 3d and Se^{2-} 3s states, respectively.[50] The presence of an Mo^{6+} peak indicates that a relatively minor amount of MoO_3 is expected to be present in the $MoSe_2$ flakes. The peak of Se around 54 eV relates to the doublet core level $3d_{5/2}$ and $3d_{3/2}$, with peak positions at 54.8 eV and 55.5 eV, respectively.

3.1. Variation in growth parameters

NaCl plays a crucial role in influencing the morphology and distribution of the $MoSe_2$ flakes. The intermediate species formed in the reaction of NaCl with MoO_3 lowers the energy barrier and decreases the reaction temperature, thereby facilitating the synthesis. The following chain of chemical reactions occurs:

$$2MoO_3 + 2NaCl \rightarrow MoO_2Cl_2\uparrow + Na_2MoO_4$$

$$3MoO_3 + 2NaCl \rightarrow MoO_2Cl_2\uparrow + Na_2Mo_2O_7$$

The MoO_3–NaCl mixture has a large weight loss at ~550 °C,[51] much lower than the melting points of MoO_3 and NaCl ($T_m(MoO_3)$ = 795 °C, T_m(NaCl) = 801 °C). Volatile MoO_2Cl_2 is one product of the reaction,[52] which sublimates at a relatively low temperature of 175 °C. The vapors of these metal oxychlorides can travel long distances to the substrates and initiate VSS (vapor–solid–solid) growth, resulting in early nucleation of TMDCs. Furthermore, some reports indicate that metal oxychlorides may undergo selenisation at a significantly faster rate than metal oxides, which enhances the reaction rate during the growth process.[25,53] Thus, the reactions of intermediate metal oxychlorides (MoO_2Cl_2), Se, and H_2 are faster and eventually facilitate the nucleation and layered growth by lowering the energetic barrier. In contrast, Na reacts with the transition metal oxides to form non-volatile molten salts (Na_xMoO_y) with high melting points (>600 °C) on the growth substrate without vapor phase transportation.[54] After reaction with chalcogen vapor, $MoSe_2$ crystals are grown from liquid melts in the VLS (vapor–liquid–solid) mode. The coexistence of the VSS and VLS induced by oxychlorides and sodium metal oxides results in an increased growth rate, large-area crystals and different morphological nanostructures. We investigated the morphological variation of the as-grown $MoSe_2$ nanocrystals as the CVD-growth parameters were changed in a methodical manner.

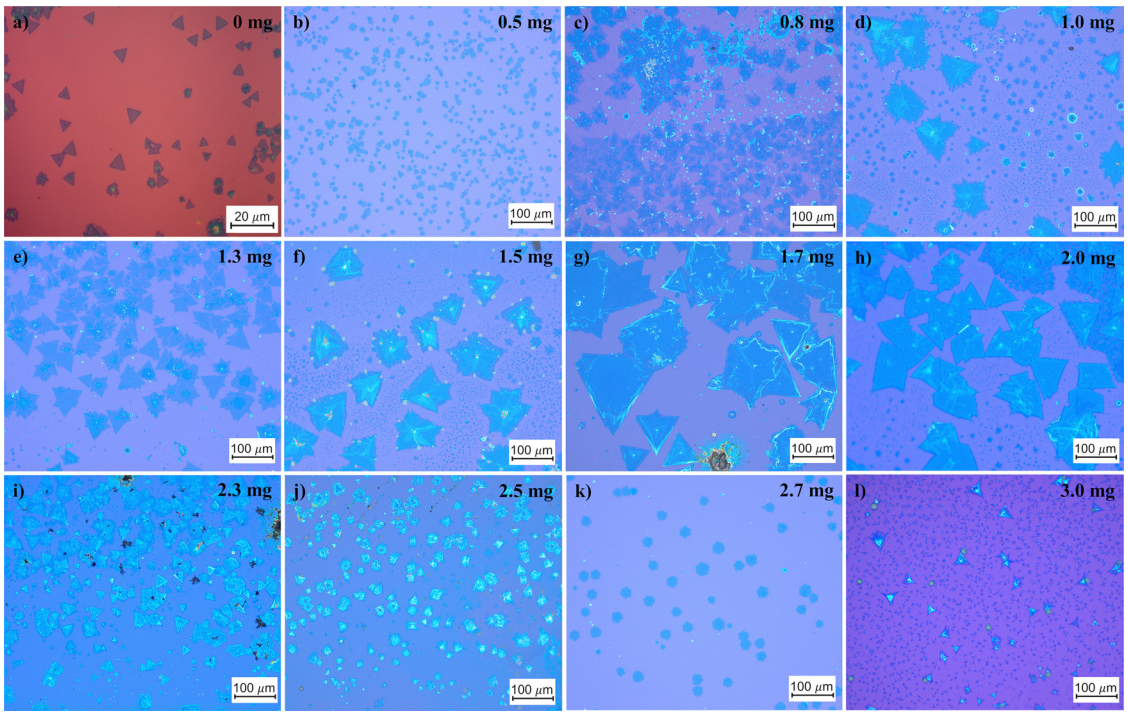

Fig. 3 High-resolution OM images showing variation in the size of the $MoSe_2$ crystal on the SiO_2/Si substrate with different amounts of NaCl. (a)–(l) Ranging from 0 to 3 mg at a growth temperature of 750 °C.

3.1.1. Amount of NaCl. $MoSe_2$ crystals were synthesised by mixing 1 mg of MoO_3 powder with different amounts of NaCl, varying it from 0.5 mg to 3 mg. With the increase in the amount of NaCl, the size of the as-grown nanocrystals increased, as shown in

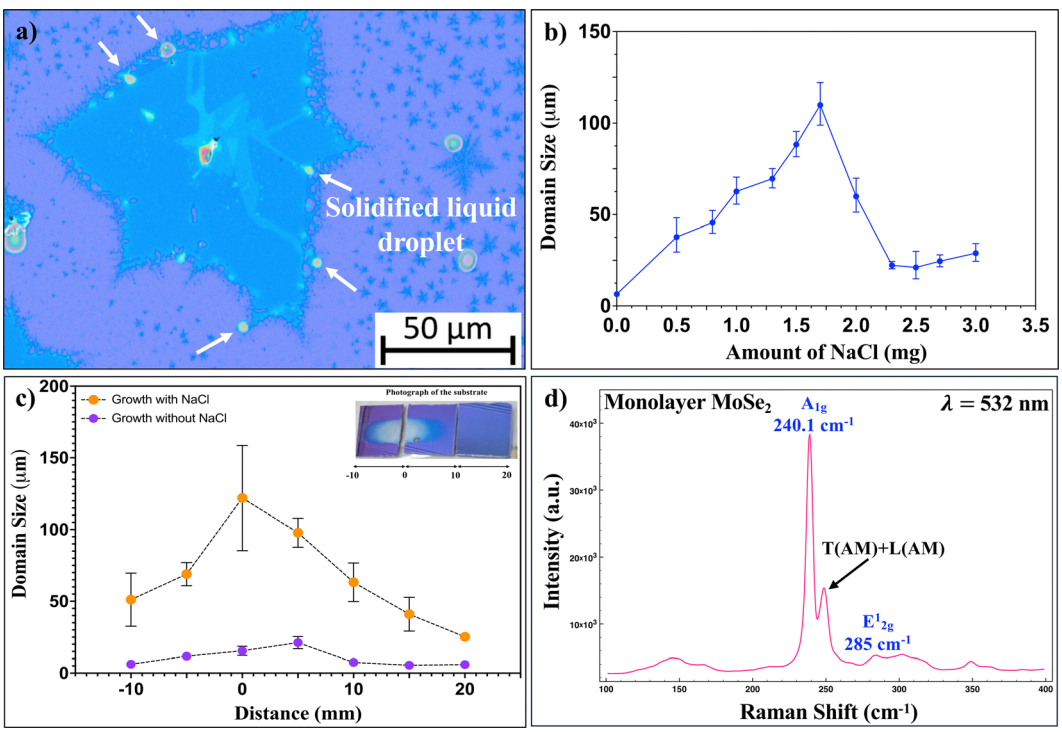

Fig. 4 (a) Optical image of the as-grown $MoSe_2$ crystal surrounded by solidified liquid droplets. (b) The domain size of $MoSe_2$ as a function of the amount of NaCl. (c) The domain size of $MoSe_2$ as a function of the distance between the metal oxide precursor and NaCl precursor to the region of deposition. (d) Raman spectrum of a monolayer $MoSe_2$ grown using NaCl.

Fig. 3. Monolayer domains were found to be predominant up to 1.3 mg of NaCl. On further increase of the amount, a large area of multilayered $MoSe_2$ regions was deposited. The optimal amount of NaCl was found to be 1.7 mg, which produced multilayered-triangular crystals with large sizes $\geq$100 μm. At higher NaCl concentrations ($\geq$1.7 mg), the lateral size of the crystals decreases significantly to 5–7 μm. NaCl acts as a fluxing agent, releasing Na and Cl species that interact with MoO_3 and Se precursors during the CVD process. The intermediate volatile species obtained in the reactions enhance the surface diffusion of Mo and Se adatoms, promoting anisotropic growth. The decrease in size at a concentration $>$1.7 mg suggests an oversaturation effect. This is because the growth environment with NaCl-derived species favours rapid nucleation, leading to suppressed lateral growth. The variation of domain size as a function of the amount of NaCl is represented graphically in Fig. 4(b), depicting a clear trend in the variation of the size of the crystals. This variation is summarised in Table S1 (ESI†). Hence, using the optimal amount of NaCl, it should be possible to deposit large-area, high-quality 2D TMDCs.

As the size of the crystals increased with the amount of NaCl, it was observed that the large area crystals were surrounded by solidified liquid droplets along the edges. This is depicted in the OM image of Fig. 4(a). These droplets attach themselves to the energy favourable sites along the edges of the as-grown crystals, serving as catalysts, enhancing the mass transport along the edges, thereby increasing the lateral size of the crystals.[17,55] In Fig. 4(c), the domain size of the crystals was plotted as a function of the distance between the metal precursor (MoO_3 + NaCl) and the position of the as-grown crystals on the substrate. Zero denotes the position of the metal oxide precursor. It is evident from the graphs that the addition of NaCl increases the size of the crystals considerably. The reduction in the size of the crystal as the distance from the source precursor increases is evident in Fig. 4(c). This is due to a concentration gradient of the Mo vapors across the substrate. The presence of such a concentration gradient is due to the fact that the local Mo : Se ratio varies along the length of the growth substrate. The crystal quality of the NaCl-assisted $MoSe_2$ crystal was determined by Raman spectroscopy (Fig. 4(d)). A_{1g} and E_{2g} peaks for monolayer $MoSe_2$ are observed at 239.9 cm^{-1} and 28 cm^{-1}, respectively. The separation, Δ, between the A_{1g} and E^1_{2g} peaks is 45.1 cm^{-1}, further confirming the monolayer nature of the crystals.[56]

XPS experiments were carried out to study the chemical composition of the $MoSe_2$ grown using NaCl. Peaks of Mo, Se, and O elements can be clearly seen in the XPS survey spectrum (Fig. 5a). Fig. 5b shows the binding energy of Na 1s located at 1072.7 eV, indicating that Na from NaCl combines with the precursor, forming intermediates such as Na_2MoO_4.[57] Fig. 5c displays energy core-level peaks located at 229.4 eV and 232.6 eV, which are attributed to Mo $3d_{5/2}$ and Mo $3d_{3/2}$ of Mo^{4+}, respectively. The Mo^{6+} 3d peak is not observed in the spectrum, indicating that the films are high-quality $MoSe_2$ and the addition of NaCl does not compromise the quality of the crystal. The peaks located at 54.9 eV and 55.8 eV correspond to the binding energies for Se $3d_{5/2}$ and Se $3d_{3/2}$, representing the Se^{2-} oxidation state (Fig. 5d).

3.1.2. Growth temperature. After fixing the optimal concentration of NaCl at 1.7 mg and keeping all the other parameters constant, the variation in growth temperature was

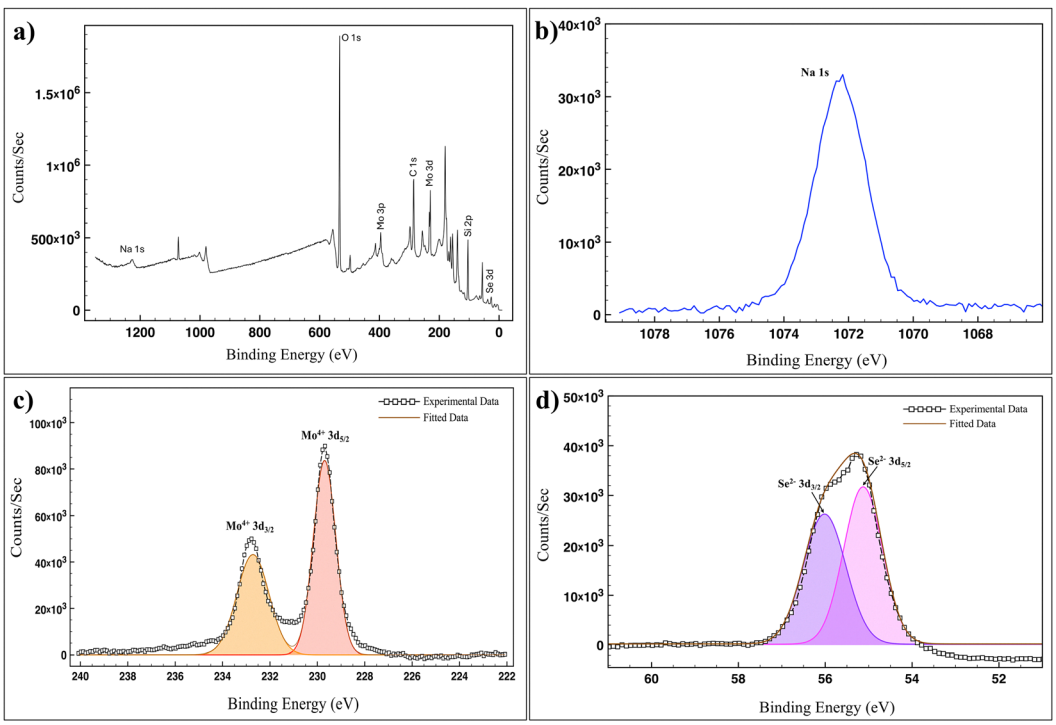

Fig. 5 XPS spectra of $MoSe_2$ monolayer grown on SiO_2/Si. (a) XPS survey spectrum. (b–d) Core-level spectra of Na 1s, Mo 3d, and Se 3d, respectively.

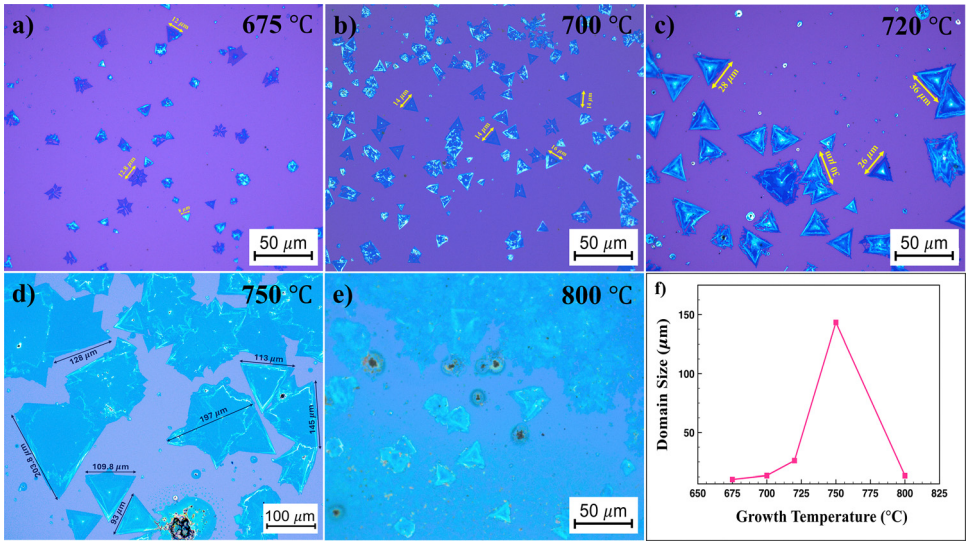

Fig. 6 High-resolution OM images showing variation in the morphology of $MoSe_2$ on SiO_2/Si at different growth temperatures using 1.7 mg of NaCl (a)–(e) ranging from 675–800 °C. (f) The domain size of $MoSe_2$ as a function of growth temperature.

studied. Fig. 6 depicts the morphological evolution of $MoSe_2$ flakes deposited at different growth temperatures. Monolayer $MoSe_2$ crystals were predominant at growth temperatures of 675 °C and 700 °C, along with the formation of some multi-layered islands. At a higher temperature of 750 °C, large-area multilayered crystals with lateral sizes of ~200 μm were observed. The nucleation density was found to increase progressively with the rise in temperature. On further increasing the temperature to 800 °C, the size of the crystals reduced drastically, and a continuous multilayered film was deposited.

The morphological evolution in the $MoSe_2$ domains on temperature can be explained by the diffusion rates of Mo, Se, and NaCl at elevated temperatures. The diffusion rate and the deposition of the MoO_3, Se, and NaCl vapors on the substrate surface vary with the change in temperature. At lower temperatures, the MoO_3 clusters deposited on the substrate's surface have a lower concentration and are small in size. At the onset of deposition, monolayers are formed on the substrate surface by reducing the MoO_3 vapors. Further deposition results in an increase in the domain size, and the $MoSe_2$ domains are thus formed with both monolayer and bilayer structures. In the case of growth at high temperatures, the high diffusion rate of the precursor results in the transport of a high concentration of nanoparticles on the surface of the substrate. This results in rapid selenisation and growth of the $MoSe_2$ crystals with the deposition of multilayer nuclei of the MoO_{3-x}-Se_y nanoparticles. Thus causing higher vapor pressure of the metal precursors and enhanced reaction rate. The further growth of these nanoparticles induces the growth of larger crystals. As the temperature is increased beyond 750 °C, the flake size decreases along with predominant multilayer deposition. The domain sizes decrease due to enhanced desorption, favouring vertical growth. Thus, 750 °C was the optimal temperature for the growth of large-area $MoSe_2$ crystals.

The Raman spectrum in Fig. 7(a) further confirms the dependence of growth temperature on the thickness of the $MoSe_2$

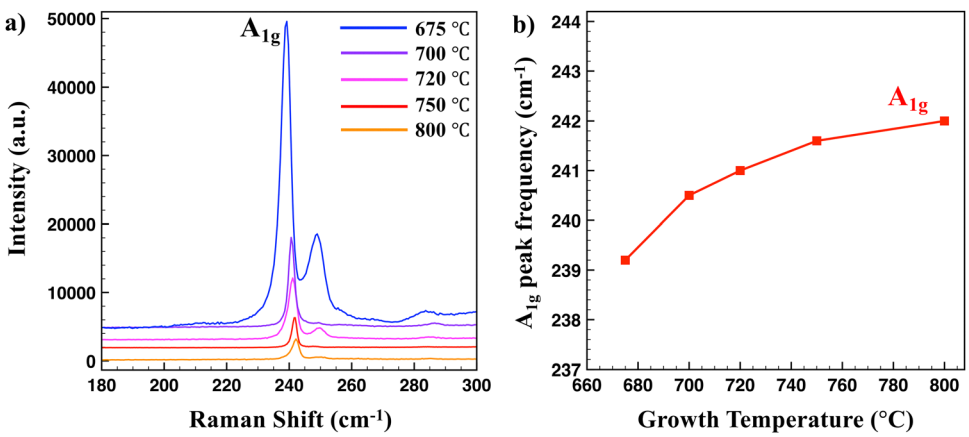

Fig. 7 (a) Temperature-dependent Raman spectra of the $MoSe_2$ crystal depicting evolution of the Raman peak; different colors represent different temperatures. (b) Frequency peaks of the A_{1g} mode plotted w.r.t. growth temperature.

films. At a growth temperature of 675 °C, the A_{1g} vibrational mode appears at 239.2 cm^{-1}, characteristic of monolayer $MoSe_2$. At 700 °C, a further shift to 240 cm^{-1} is observed. Consequently, with increasing growth temperature, a blue shift in the A_{1g} peak is observed (as plotted in Fig. 7(b)), indicating an increase in the film thickness.[58,59] At 800 °C, a maximum shift of 3 cm^{-1} is measured. This is consistent with the formation of multilayer $MoSe_2$. The low-intensity E_{1g} peak at ~283.4 cm^{-1} diminishes considerably with increasing thickness. The effects of the growth temperature on the morphology of the $MoSe_2$ crystals are summarised in Table S2 (ESI†).

3.1.3. Amount of Se precursor. Besides growth temperature, the Mo : Se ratio is the primary criterion affecting the growth of TMDCs. Here, we investigated the effect of Se concentration on the growth of $MoSe_2$ films while keeping the NaCl amount and growth temperatures fixed at 1.7 mg and 750 °C, respectively. By controlling the Se vapor pressure, the as-grown atomic crystals undergo a three-stage shape transformation from fractals and dendrite deposition to 2D compact nanocrystals and eventually to nanoribbons, as illustrated by the flowchart in Fig. 8.

At lower Se concentration (150 mg), fractal and dendritic crystals with thick branches were observed. The size of these crystals varies, with a maximum length of ~100 μm. At higher Se concentrations (300 mg), the gaseous atmosphere becomes enriched with Se and Mo. More Se atoms reach the substrate, resulting in compact triangular crystal structures. When the concentration of Se is further increased to 600 mg, nanoribbons with lengths ≥100 μm were observed. Preferential growth of the nanoribbons along the edges of the triangular $MoSe_2$ domains was predominant. The variation in morphology with Se concentration is summarised in Table S3 (ESI†).

The analysis of XPS data to study the stoichiometry of these crystals is reported in the ESI† (Section S2). The high-resolution deconvoluted XPS spectra of Mo 3d and Se 3d peaks of crystals grown at 150 mg, 300 mg and 600 mg Se concentrations are shown in Fig. S1, S2 and S3 (ESI†), respectively. The Mo : Se ratio for the dendritic crystals was determined to be ~0.47, corresponding to a Se-deficient condition. This sub-stoichiometric composition can also be ascribed to Se vacancies.[56] This ratio for the triangular crystals was found to be 0.5, which is congruent with the literature. Whereas, for the nanoribbons, the value of the Mo : Se ratio was ~0.67, corresponding to a Se-rich environment. The details of these calculations are reported in Table S4 (ESI†).

3.2. Morphological evolution

On systematic variation of the growth parameters, diverse nanostructures were deposited. Among them, nanoribbons were dominant. The transition from fractals to snowflakes and

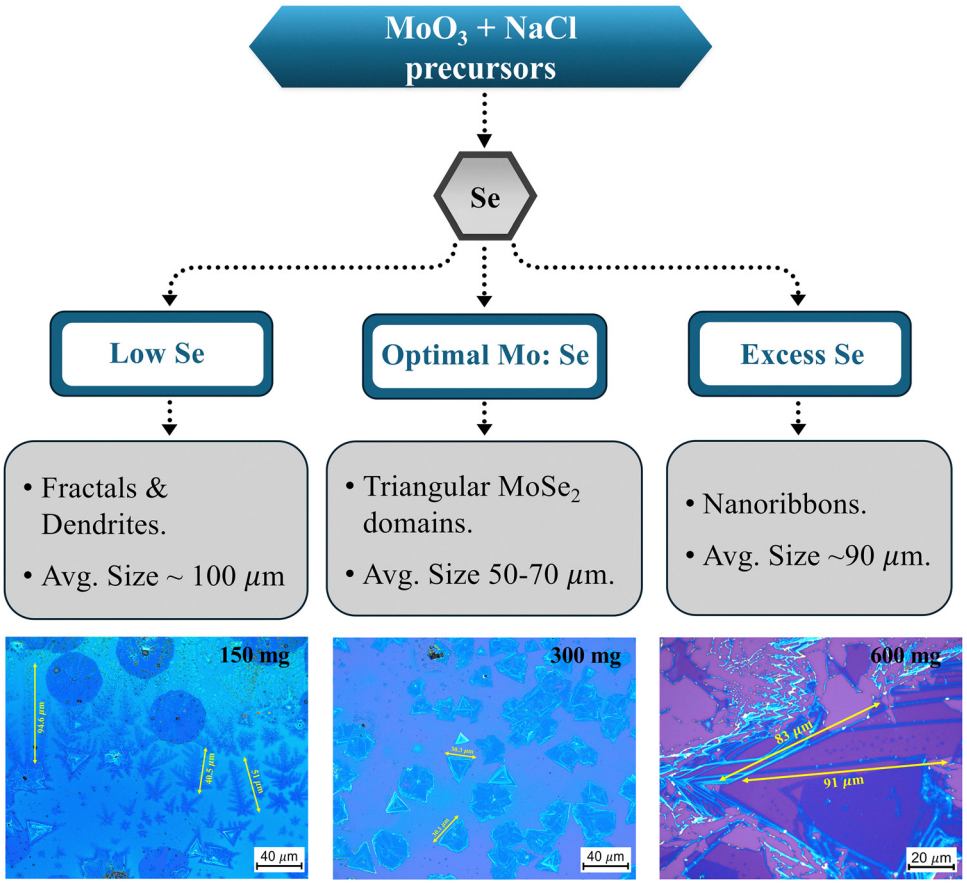

Fig. 8 Flowchart illustrating the change in morphology of $MoSe_2$ crystals with varied amounts of Se precursor.

dendrites was also prevalent. In addition, spiral growth on $MoSe_2$ triangular domains was found. The growth mechanism of these nanostructures is discussed in the following subsections.

3.2.1. Nanoribbons. The growth of nanoribbons can be explained by the vapour–liquid–solid (VLS) mechanism.

In the synthesis process, the precursors evaporate and undergo a chemical reaction between the vapors of MoO_3 and NaCl, forming intermediate species like Na_2MoO_4/Na_2MoO_7.[33] A mixture of gas–liquid droplets is formed when these intermediate species diffuse and melt on the substrate. Vaporised Se dissolves into the droplet continuously and results in the formation of $MoSe_2$ seeds. As the droplet crawls on the surface, Se continues to dissolve into the droplet, inducing further growth and yielding ribbon-like structures.[60] In the XPS data (Fig. S4 and S5, ESI†), the Na 1s peak is observed at 1071.69 eV corresponding to Na_2MoO_x,[61] which confirms the presence of intermediate Na–Mo compounds on the surface. This peak intensifies at higher growth temperatures, namely 750 °C. This was also the optimal temperature for the CVD growth of long $MoSe_2$ nanoribbons in our studies. This further gives evidence of the role of intermediate species in the growth of nanoribbons.

The average length of the nanoribbons was measured to be ~70 μm, with a maximum length of ~120 μm. The lengths vary with the amount of NaCl mixed with the MoO_3 precursor. It was found that the growth of nanoribbons was initiated with NaCl concentration greater than 1.3 mg. The length increases with increase in NaCl concentration, reaching a saturation point. Beyond this, there is no effect on the length of the nanoribbons with the addition of NaCl. This observation is congruent with the variation in the size of the crystals with NaCl concentration. The variation in the average nanoribbon length as a function of NaCl amount is shown in Fig. 9(e). The growth of nanoribbons observed in this study is predominantly along the edges of the underlying domain, as evident from Fig. 9(a) and (f).

The alignment of these ribbons is primarily determined by the orientation of the underlying crystal. Additionally, few-layered nanoribbons extending from the nucleation site on the $MoSe_2$ domain are observed as shown in the high resolution OM images of Fig. 9(b) and (c). These ribbons are locally aligned but exhibit occasional regular kinks, suggesting that the growth is guided either by the substrate or the crystal facets of the underlying $MoSe_2$ domain. It is observed that some of the

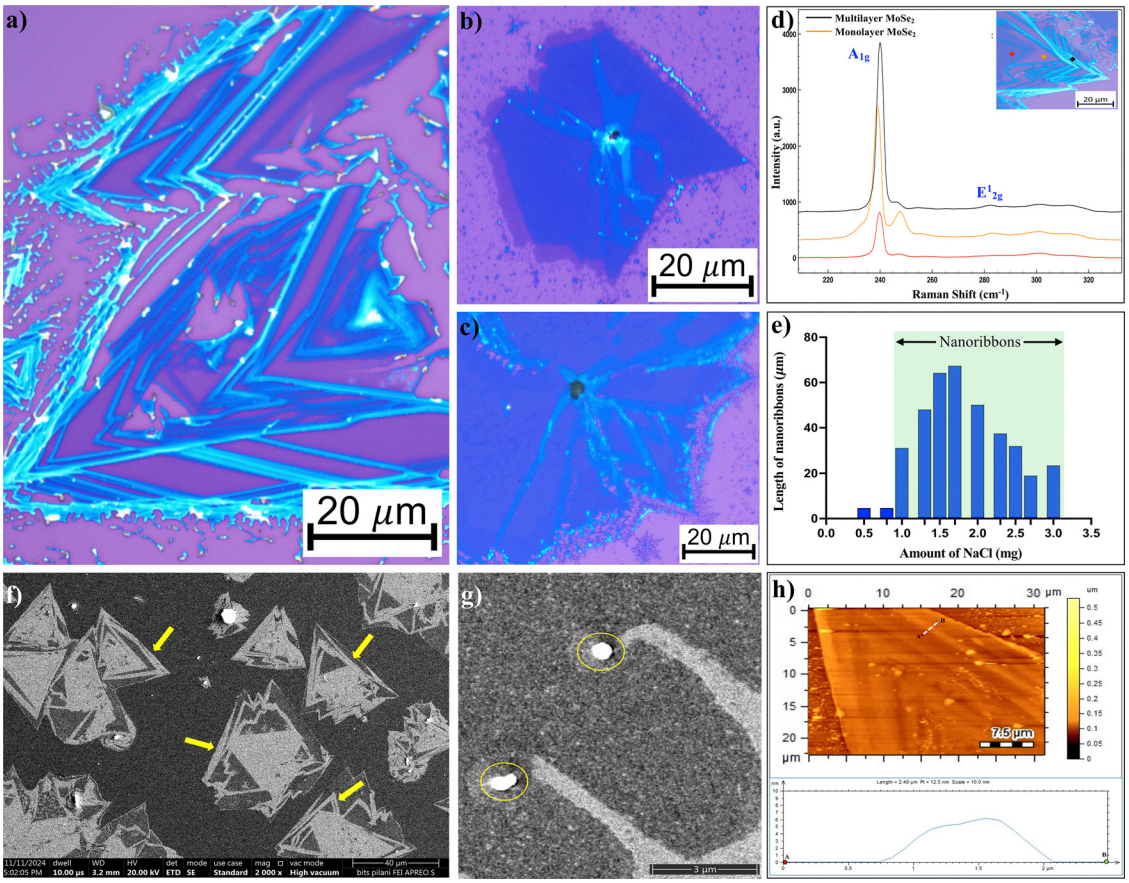

Fig. 9 (a)–(c) are high-resolution OM images of $MoSe_2$ nanoribbons. (d) Raman data of the nanoribbons. (e) Plot showing variation in the length of the nanoribbons w.r.t. the amount of NaCl used. FESEM images showing (f) nanoribbons grown along the edges of the $MoSe_2$ crystals, indicated by yellow arrows; (g) zoomed-in image with an encircled nanoparticle; (h) AFM image and height profile (along the line AB) of the as-grown $MoSe_2$ nanoribbons.

nanoribbons are terminated with a nanoparticle. Fig. 9(g) shows a zoomed-in FESEM image of such nanoparticles. The size of these particles is measured to match with that of the width of the ribbons (~0.14 μm). As mentioned earlier, these characteristic features of nanostructures result from the crawling mode of VLS growth. For a few nanoribbons, there were no nanoparticles at their ends. In some cases, the absence of the nanoparticle can be explained by the fact that the liquid droplet precursor might have been consumed during the growth of the ribbon. Fig. 9(d) shows the Raman measurement of the nanoribbons grown on triangular $MoSe_2$ domains. The difference between A_{1g} and E_{2g} ($\Delta = 42\ cm^{-1}$) in the data confirms that the multilayer nanoribbons are grown on few-layer $MoSe_2$ domains. AFM measurements were acquired to study the surface morphology and the thickness of the $MoSe_2$ nanoribbons. Fig. 9(h) depicts the AFM image and the height profile of a nanoribbon scanned in the non-contact mode, respectively. The contrast in the image indicates the difference in the heights of the structure. A height profile along the line AB denotes a thickness of ~6 nm, corresponding to a thickness of around 10 layers.

3.2.2. Fractals-snowflakes-dendrites. A transition from compact triangles to fractal to dendritic deposition was observed under certain growth conditions. We observed the growth of fractals and snowflakes at a 1 mg concentration of NaCl (Mo : Se = 1 mg : 600 mg), but thick-branched dendrite structures were observed at a low Se concentration (Mo : Se = 1 mg : 150 mg). In Fig. 10(a) and (b), a clear transition from the compact island to fractals at the edges is observed.

At increased flux of metal precursor, the dominant morphology is fractal due to surface diffusion prevailing over edge diffusion.[62] The adatoms reaching the edge of growing triangular domains do not contribute to the lateral growth. They diffuse randomly, which leads to the formation of fractals. The edge diffusion is highly suppressed, but the incoming adatoms attach themselves to the domain edges predominantly *via* diffusion-limited aggregation (DLA).[63] Adding NaCl as a seed promoter, there is an obvious increase in the metal flux because of the increase in volatile metal oxychlorides (MoO_xCl_y). Thus, the formation of fractals along the edges of a compact triangular domain and that of isolated fractals are promoted.

The transition from triangular to truncated, and further to fractal and dendritic $MoSe_2$ flakes, is attributed[64,65] to accelerated directional growth of either a Mo- or Se-terminated edge under a Se-deficient or Mo-rich growth environment, respectively. Thus, different dendritic shapes are induced, including snowflakes. Dendritic structures are observed at a low Se concentration, mainly at the substrate–boat contact interface, which creates a confined space leading to a high flux of metal precursors.[61,66] The abundance of MoO_{3-x} vapour in the confined reaction space also leads to fractal edges surrounding the compact triangular flakes, as shown in the AFM image of Fig. 10(c). The fractal edges observed in our experiment could be understood to be driven by kinetics rather than thermodynamics. This is congruent with our earlier work on MoS_2 dendrites.[38] These dendrites develop as atoms and diffuse preferentially along specific directions, forming the characteristic "branches" of the structure. From Fig. 10(d), it can be observed that most of the dendrites align with the three crystallographic directions typical of snowflakes. The larger dendrites have a greater number of branches, as shown in Fig. 10(e) and (f). The anisotropic influence of neighbouring atoms, combined with the tendency of dendrites to grow only along lower-energy directions, causes their preferential growth along specific directions.

3.2.3. Spiral growth. In addition to different morphologies, the growth of spiral $MoSe_2$ pyramids was observed. The contrast in the optical image of spiral $MoSe_2$ in Fig. 11 indicates that the thickness increases from the edge to the centre of spiral $MoSe_2$. The size of these domains ranges from 50 μm to 80 μm.

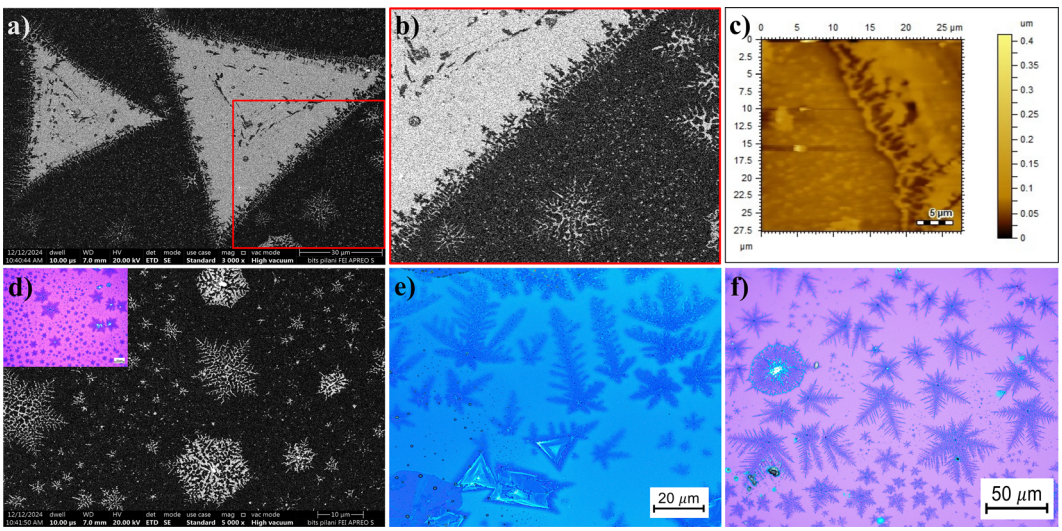

Fig. 10 (a) FESEM image of a $MoSe_2$ crystal with fractal edges. (b) Zoomed-in image of the area enclosed in a red square showing the fractals near the edges in Fig. 9(a). (c) AFM image showing the fractal edge of a triangular crystal. (d) FESEM images of snowflakes, inset contains a high-resolution OM image of the same. (e) and (f) High-resolution OM images of the as-grown $MoSe_2$ dendrite structures.

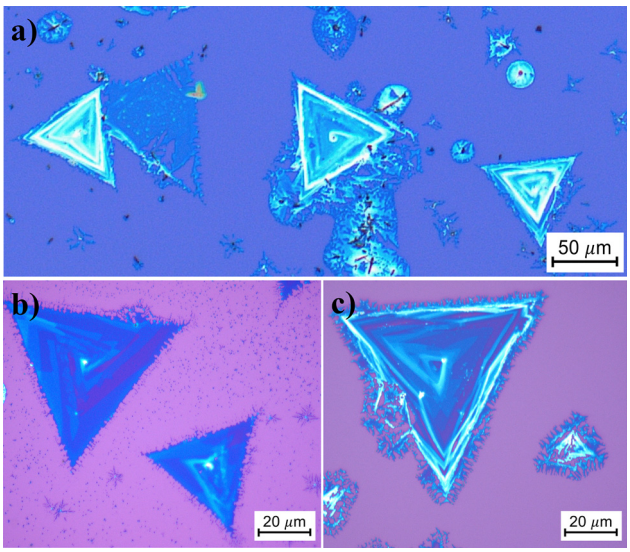

Fig. 11 (a)–(c) High-resolution OM images showing a spiral $MoSe_2$ pyramid.

The formation of the spiral growth depends on the $MoSe_2$ flux. At low $MoSe_2$ flux, monolayer $MoSe_2$ is formed, whereas, as the flux increases, both monolayer and spiral $MoSe_2$ are obtained. At a high flux of $MoSe_2$, thick spiral $MoSe_2$ with screw dislocations is formed. A diffusion-limited growth mechanism causes the formation of a domain when it is growing. During this growth, one grain boundary can elevate over another when two edges encounter a lattice mismatch within the same domain.[42] A line of unsaturated chalcogen dangling bonds is formed on the lifted edge. A screw dislocation appears at the end of this line, which favours the growth of spirals. The generation of screw dislocations is thus increased, if the probability of a misaligned meeting of two exposed edges is increased. These accidental overgrowths occur frequently when the 2D growth rate increases. The rapid growth of certain edges is thus favoured over slower ones, when the growth rate is high. The spiral growth is observed in the as-grown $MoSe_2$ crystals on adding NaCl with amounts $\geq$1.3 mg at a growth temperature of 750 °C. The considerable increase in growth rate when adding salt promotes the formation of edge dislocations. As growth advances around the screw dislocation, the exposed edges trace the corners of the underlying layer edges. This leads to the formation of the spirals.

4. Conclusions

The controlled growth of diverse $MoSe_2$ nanostructures synthesised using an APCVD was systematically investigated, with NaCl serving as a seed promoter. Key CVD growth parameters, including the optimal NaCl concentration, growth temperature, and chalcogen precursor amount, were optimised to grow unique morphologies such as nanoribbons, dendrites, snowflakes, and spirals. A morphological mapping of a clearly defined parameter space is proposed to grow the desired nanostructures. This study not only establishes precise conditions for the reproducible synthesis of these unique structures but also provides insights into their growth mechanisms. This comprehensive study can be extended to the controlled CVD growth of various other TMDC nanostructures to be used in various next-generation applications.

Data availability

The data that support the findings of this study are available from the corresponding author upon reasonable request.

Conflicts of interest

The authors declare that they have no known competing financial interests or personal relationships that could have appeared to influence the work reported in this paper.

Acknowledgements

We would like to express our sincere gratitude to Dr Krishnendu Chatterjee for his invaluable contribution to the development of the QRYSTAL CVD. We sincerely thank Mr Sandeep Kumar for his assistance in synthesizing CVD $MoSe_2$. Additionally, we extend our heartfelt thanks to Dr O. P. Thakur, Solid State Physics Laboratory (SSPL), DRDO, Timarpur, Delhi, for granting us access to their microscopy facility and to Dr Akhilesh Pandey, SSPL, DRDO, for providing the AFM facility. We thank Garima Gupta (SSPL, DRDO) for acquiring AFM data. We thank the SIF facility, BITS Pilani, and Pilani Campus, for providing FESEM, XPS and Raman facilities.

References

1 S. Zhang, Y. Hao, F. Gao, X. Wu, S. Hao, M. Qiu, X. Zheng, Y. Wei and G. Hao, Controllable growth of wafer-scale two-dimensional WS_2 with outstanding optoelectronic properties, *2D Mater.*, 2023, **11**(1), 015007.
2 W. Yan, J. Wan, B. Zhao, Z. Zhang, L. Meng and X. A. Li, Controllable Synthesis of Large-Area $MoSe_2$ Monolayer Films and Bilayer Crystals, *J. Phys. Chem. C*, 2024, **128**, 58.
3 W. Fu, M. John, T. D. Maddumapatabandi, F. Bussolotti, Y. S. Yau, M. Lin and K. E. Johnson Goh, Toward Edge Engineering of Two-Dimensional Layered Transition-Metal Dichalcogenides by Chemical Vapor Deposition, *ACS Nano*, 2023, **17**(17), 16348–16368.
4 J. D. Cain, F. Shi, J. Wu and V. P. Dravid, Growth Mechanism of Transition Metal Dichalcogenide Monolayers: The Role of Self-Seeding Fullerene Nuclei, *ACS Nano*, 2016, **10**(5), 5440–5445.
5 T. Chen, G. Hao, G. Wang, B. Li, L. Kou, H. Yang, X. Zheng and J. Zhong, Controlled growth of atomically thin $MoSe_2$ films and nanoribbons by chemical vapor deposition, *2D Mater.*, 2019, **6**(2), 025002.
6 J. Huang, H. Liu, B. Jin, M. Liu, Q. Zhang, L. Luo, S. Chu, S. Chu and R. Peng, Large-area snow-like $MoSe_2$

monolayers: synthesis, growth mechanism, and efficient electrocatalyst application, *Nanotechnology*, 2017, **28**(27), 275704.

7 Y. H. Chang, W. Zhang, Y. Zhu, Y. Han, J. Pu, J. K. Chang, W. T. Hsu, J. K. Huang, C. L. Hsu, M. H. Chiu, T. Takenobu, H. Li, C. I. Wu, W. H. Chang, A. T. S. Wee and L. J. Li, Monolayer $MoSe_2$ grown by chemical vapor deposition for fast photodetection, *ACS Nano*, 2014, **8**(8), 8582–8590.

8 A. Eftekhari, Molybdenum diselenide ($MoSe_2$) for energy storage, catalysis, and optoelectronics, *Appl. Mater. Today*, 2017, **8**, 1–17.

9 S. Li, Salt-assisted chemical vapor deposition of two-dimensional transition metal dichalcogenides, *iScience*, 2021, **11**(24), 103229.

10 J. C. Shaw, H. Zhou, Y. Chen, N. O. Weiss, Y. Liu, Y. Huang and X. Duan, Chemical vapor deposition growth of monolayer $MoSe_2$ nanosheets, *Nano Res.*, 2014, **7**, 511–517.

11 X. Lu, M. I. B. Utama, J. Lin, X. Gong, J. Zhang, Y. Zhao, S. T. Pantelides, J. Wang, Z. Dong, Z. Liu, W. Zhou and Q. Xiong, Large-area synthesis of monolayer and few-layer $MoSe_2$ films on SiO_2 substrates, *Nano Lett.*, 2014, **14**(5), 2419–2425.

12 J. Xia, X. Huang, L. Z. Liu, M. Wang, L. Wang, B. Huang, D. D. Zhu, J. J. Li, C. Z. Guc and X. M. Meng, CVD synthesis of large-area, highly crystalline $MoSe_2$ atomic layers on diverse substrates and application to photodetectors, *Nanoscale*, 2014, **6**(15), 8949–8955.

13 Z. Chen, H. Liu, X. Chen, G. Chu, S. Chu and H. Zhang, Wafer-size and single-crystal $MoSe_2$ atomically thin films grown on GaN substrate for light emission and harvesting, *ACS Appl. Mater. Interfaces*, 2016, **8**(31), 20267–20273.

14 Y. Zhao, H. Lee, W. Choi, W. Fei and C. J. Lee, Large-area synthesis of monolayer $MoSe_2$ films on SiO_2/Si substrates by atmospheric pressure chemical vapor deposition, *RSC Adv.*, 2017, **7**(45), 27969–27973.

15 H. Wang, D. Zhu, F. Jiang, P. Zhao, H. Wang, Z. Zhang, X. Chen and C. Jin, Revealing the microscopic CVD growth mechanism of $MoSe_2$ and the role of hydrogen gas during the growth procedure, *Nanotechnology*, 2018, **29**, 31.

16 T. Pham, K. Reidy, J. D. Thomsen, B. Wang, N. Deshmukh, M. A. Filler and F. M. Ross, Salt-assisted vapor-liquid-solid growth of 1D van der Waals, *Materials*, 2024, **36**(24), 2309360.

17 S. Yang, C. Wang, J. Wu, H. Yan, G. Wang, J. Feng, B. Zhang, D. Li, T. J. Booth, P. Bøggild, G. Yu and B. Luo, Self-relaxation vapor-liquid-solid growth of two-dimensional transition metal dichalcogenides with loose interface, *Appl. Surf. Sci.*, 2023, **613**, 156019.

18 H. Guo, Y. Xu, H. Chen, Z. Wang, X. Mao, G. Zhou, J. Zhang and S. Wang, Synthesis of multiwall Boron Nitride (BN) nanotubes by a PVD method based on vapor-liquid-solid Growth, *Materials*, 2020, **13**(4), 915.

19 Y. Hacohen, R. Popovitz-Biro, E. Grunbaum, Y. Prior and R. Tenne, Vapor-liquid-solid growth of $NiCl_2$ nanotubes *via* reactive gas laser ablation, *Adv. Mater.*, 2002, **14**(15), 1075–1078.

20 G. Shao, X. X. Xue, X. Zhou, J. Xu, Y. Jin, S. Qi, N. Liu, H. Duan, S. Wang, S. Li, M. Ouzounian, T. S. Hu, J. Luo, S. Liu and Y. Feng, Shape-engineered synthesis of atomically thin 1T-SnS_2 catalyzed by potassium halides, *ACS Nano*, 2019, **13**(7), 8265–8274.

21 P. Schönherr, L. J. Collins-McIntyre, S. L. Zhang, P. Kusch, S. Reich, T. Giles, D. Daisenberger, D. Prabhakaran and T. Hesjedal, Vapour-liquid-solid growth of ternary Bi_2Se_2Te nanowires, *Nanoscale Res. Lett.*, 2014, **9**(1), 1–6.

22 S. Li, S. Wang, D. M. Tang, W. Zhao, H. Xu, L. Chu, Y. Bando, D. Golberg and G. Eda, Halide-assisted atmospheric pressure growth of large WSe_2 and WS_2 monolayer crystals, *Appl. Mater. Today*, 2015, **1**(1), 60–66.

23 S. Li, Y. C. Lin, J. Hong, B. Gao, H. E. Lim and X. Yang, *et al.*, Mixed-Salt Enhanced Chemical Vapor Deposition of Two-Dimensional Transition Metal Dichalcogenides, *Chem. Mater.*, 2021, 33.

24 H. Kim, D. Ovchinnikov, D. Deiana, D. Unuchek and A. Kis, Suppressing nucleation in metal-organic chemical vapor deposition of MoS_2 monolayers by alkali metal halides, *Nano Lett.*, 2017, **17**(8), 5056–5063.

25 J. Zhou, J. Lin, X. Huang, Y. Zhou, Y. Chen, J. Xia, H. Wang, Y. Xie, H. Yu, J. Lei, D. Wu, F. Liu, Q. Fu, Q. Zeng, C. H. Hsu, C. Yang, L. Lu, T. Yu, Z. Shen, H. Lin, B. I. Yakobson, Q. Liu, K. Suenaga, G. Liu and Z. Liu, A library of atomically thin metal chalcogenides, *Nature*, 2018, **556**, 355–359.

26 J. Li, W. Yan, Y. Lv, J. Leng, D. Zhang, C. O. Coileaín, C. P. Cullen, S. T. Lindner, G. S. Duesberg, J. Cho, M. Choi, B. S. Chun, Y. Zhao, C. Lv, S. K. Arora and H. C. Wu, Sub-millimeter size high mobility single crystal $MoSe_2$ monolayers synthesized by NaCl-assisted chemical vapor deposition, *RSC Adv.*, 2020, **10**(3), 1580–1587.

27 Q. Feng, M. Zhu, Y. Zhao, H. Liu, M. Li, J. Zheng, H. Xu and Y. Jiang, Chemical vapor deposition growth of sub-centimeter single crystal WSe_2 monolayer by NaCl-assistant, *Nanotechnology*, 2019, **30**, 3.

28 A. Singh, M. Moun, M. Sharma, A. Barman, A. Kumar Kapoor and R. Singh, NaCl-assisted substrate dependent 2D planar nucleated growth of MoS_2, *Appl. Surf. Sci.*, 2021, **538**, 148201.

29 M. Bay, Y. Çelik, F. Ay and N. K. Perkgöz, Catalytic strategies for uniform monolayer $MoSe_2$ growth in CVD processes, *Mater. Sci. Semicond. Process.*, 2024, **180**, 108551.

30 P. Cui, J. H. Choi, W. Chen, J. Zeng, C. K. Shih, Z. Li and Z. Zhang, Contrasting structural reconstructions, electronic properties, and magnetic orderings along different edges of zigzag transition metal dichalcogenide nanoribbons, *Nano Lett.*, 2017, **17**(2), 1097–1101.

31 Y. Chen, P. Cui, X. Ren, C. Zhang, C. Jin, Z. Zhang and C. K. Shih, Fabrication of $MoSe_2$ nanoribbons *via* an unusual morphological phase transition, *Nat. Commun.*, 2017, **8**(1), 1–9.

32 S. M. Poh, S. J. R. Tan, X. Zhao, Z. Chen, I. Abdelwahab, D. Fu, H. Xu, Y. Bao, W. Zhou and K. P. Loh, Large area synthesis of 1D-$MoSe_2$ using molecular beam epitaxy, *Adv. Mater.*, 2017, **29**(12), 1605641.

33 Y. Li, Z. Zhou, S. Zhang and Z. Chen, MoS_2 nanoribbons: High stability and unusual electronic and magnetic properties, *J. Am. Chem. Soc.*, 2008, **130**(49), 16739–16744.
34 Q. Zhou, S. Su, P. Cheng, X. Hu, X. Gao, Z. Zhang and J. M. Liu, Vertically conductive MoS_2 pyramids with a high density of active edge sites for efficient hydrogen evolution, *J. Mater. Chem. C*, 2020, **8**, 3017.
35 X. Xu and L. Liu, MoS_2 with Controlled thickness for electrocatalytic hydrogen evolution, *Nanoscale Res. Lett.*, 2021, **16**(1), 1–10.
36 Y. Zhang, K. Liu, F. Wang, T. A. Shifa, Y. Wen, F. Wang, K. Xu, Z. Wang, C. Jiang and J. He, Dendritic growth of monolayer ternary $WS_{2(1-x)}Se_{2x}$ flakes for enhanced hydrogen evolution reaction, *Nanoscale*, 2017, **9**(17), 5641–5647.
37 J. Xie, H. Zhang, S. Li, R. Wang, X. Sun, M. Zhou, J. Zhou, X. W. Lou and Y. Xie, Defect-rich MoS_2 ultrathin nanosheets with additional active edge sites for enhanced electrocatalytic hydrogen evolution, *Adv. Mater.*, 2013, **25**(40), 5807–5813.
38 M. Tyagi, A. A. Tiwari, S. Dey and D. Sahdev, Chemical vapor deposition growth ofs large-area molybdenum disulphide (MoS_2) dendrites, *Nano-Struct. Nano-Objects*, 2024, **40**, 101380.
39 T. H. Ly, J. Zhao, H. Kim, G. H. Han, H. Nam and Y. H. Lee, Vertically Conductive MoS_2 Spiral Pyramid, *Adv. Mater.*, 2016, **28**(35), 7723–7728.
40 J. Ahn, S. Ha, J. Choi, D. I. Yeom and Y. Yoo, Large-area structure selective synthesis of symmetry-broken $MoSe_2$ and their broadband nonlinear optical response, *Adv. Opt. Mater.*, 2023, **11**, 12.
41 D. Ouyang, X. Tong, S. Liu, J. Wang, Y. Zhao, R. Liu, X. Zhao, N. Zhang, F. Cao, Y. Liu, Y. Li, L. Li and T. Zhai, Superior nonlinear optical response in non-centrosymmetric stacking edge-rich spiral $MoTe_2$ nanopyramids, *Adv. Funct. Mater.*, 2022, **32**(21), 2113052.
42 X. Fan, Y. Jiang, X. Zhuang, H. Liu, T. Xu, W. Zheng, P. Fan, H. Li, X. Wu, X. Zhu, Q. Zhang, H. Zhou, W. Hu, X. Wang, L. Sun, X. F. Duan and A. Pan, Broken symmetry induced strong nonlinear optical effects in spiral WS_2 nanosheets, *ACS Nano*, 2017, **11**(5), 4892–4898.
43 M. J. Shearer, L. Samad, Y. Zhang, Y. Zhao, A. Puretzky, K. W. Eliceiri, J. C. Wright, R. J. Hamers and S. Jin, Complex and non-centrosymmetric stacking of layered metal dichalcogenide materials created by screw dislocations, *J. Am. Chem. Soc.*, 2017, **139**(9), 3496–3504.
44 QRYSTAL-CVD-1100 Chemical Vapour Deposition System Specification sheet.
45 Quazar Technologies Pvt. Ltd, **https://quazartech.com/**.
46 P. Soubelet, A. E. Bruchhausen, A. Fainstein, K. Nogajewski and C. Faugeras, Resonance effects in the Raman scattering of monolayer and few-layer $MoSe_2$, *Phys. Rev. B*, 2016, **93**, 15.
47 P. Tonndorf, R. Schmidt, P. Böttger, X. Zhang, J. Börner, A. Liebig, M. Albrecht, C. Kloc, O. Gordan, D. R. T. Zahn, S. Michaelis de Vasconcellos and R. Bratschitsch, Photoluminescence emission and Raman response of monolayer MoS_2, $MoSe_2$ and WSe_2, *Opt. Express*, 2013, **21**(4), 4908.
48 P. A. Markeev, E. Najafidehaghani, Z. Gan, K. Sotthewes, A. George, A. Turchanin and M. P. Jong, Energy-level alignment at interfaces between transition-metal dichalcogenide monolayers and metal electrodes studied with kelvin probe force microscopy, *J. Phys. Chem. C*, 2021, **125**(24), 13551–13559.
49 S. Wang, G. Wang, X. Yang, H. Yang, M. Zhu, S. Zhang, G. Peng and Z. Li, Synthesis of monolayer $MoSe_2$ with controlled nucleation *via* reverse-flow chemical vapor deposition, *Nanomaterials*, 2020, **10**(1), 75.
50 G. S. Papanai, K. R. Sahoo, G. B. Reshma, S. Gupta and B. K. Gupta, Role of processing parameters in CVD grown crystalline monolayer $MoSe_2$, *RSC Adv.*, 2022, **12**(21), 13428–13439.
51 M. Mobin, A. U. Malik and S. Ahmad, High-temperature interactions of metal oxides with NaCl, *J. Less-Common Met.*, 1990, **160**(1), 1–14.
52 D. A. Johnson, J. H. Levy, J. C. Taylor, A. B. Waugh and J. Brough, Purification of molybdenum: volatilisation processes using MoO_3, *Polyhedron*, 1982, **1**(5), 479–482.
53 X. R. Shi, J. Wang and K. Hermann, Theoretical cluster studies on the catalytic sulfidation of MoO_3, *J. Phys. Chem. C*, 2010, **114**(14), 6791–6801.
54 H. R. Rasouli, N. Mehmood, O. Çakiroğlu and T. Serkan Kasirga, Real-time optical observation and control of atomically thin transition metal dichalcogenide synthesis, *Nanoscale*, 2019, **11**(15), 7317–7323.
55 L. Huang, Q. H. Thi, F. Zheng, X. Chen, Y. W. Chu, C. S. Lee, J. Zhao and T. H. Ly, Catalyzed Kinetic Growth in Two-Dimensional MoS_2, *J. Am. Chem. Soc.*, 2020, **142**(30), 13130–13135.
56 C. González, J. P. B. Silva, A. S. Viana, K. Gwozdz and O. Conde, Shape-controlled monolayer $MoSe_2$ flakes by chemical vapor deposition towards tuning the photoluminescence emission, *Appl. Surf. Sci.*, 2022, **605**, 154742.
57 L. Chen, L. Zang, L. Chen, J. Wu, C. Jiang and J. Song, Study on the catalyst effect of NaCl on MoS_2 growth in a chemical vapor deposition process, *Cryst. Eng. Commun.*, 2021, **23**(31), 5337.
58 X. Zhang, Characterization of Layer Number of Two-Dimensional Transition Metal Diselenide Semiconducting Devices Using Si-Peak Analysis, *Adv. Mater. Sci. Eng.*, 2019, (1), 7865698.
59 Y. Sha, S. Xiao, X. Zhang, F. Qin and X. Gu, Layer-by-layer thinning of $MoSe_2$ by soft and reactive plasma etching, *Appl. Surf. Sci.*, 2017, **411**, 182–188.
60 S. Li, Y. C. Lin, W. Zhao, J. Wu, Z. Wang, Z. Hu, Y. Shen, D. M. Tang, J. Wang, Q. Zhang, H. Zhu, L. Chu, W. Zhao, C. Liu, Z. Sun, T. Taniguchi, M. Osada, W. Chen, Q. H. Xu, A. T. S. Wee, K. Suenaga, F. Ding and G. Eda, Vapor-liquid-solid growth of monolayer MoS_2 nanoribbons, *Nat. Mater.*, 2018, **17**, 535–542.
61 R. R. Srivastava, S. Sarkar and A. Srivastava, Study of morphological evolution and growth mechanism of CVD grown 2D tin disulfide, *Surf. Interfaces*, 2023, **38**, 102870.
62 J. Ren, B. Guo, Y. Feng and K. Yu, Few-layer MoS_2 dendrites as a highly active humidity sensor, *Phys. E*, 2020, **116**, 113782.
63 S. Chowdhury, A. Roy, I. Bodemann and S. K. Banerjee, Two-dimensional to three-dimensional growth of transition metal diselenides by chemical vapor deposition: interplay between fractal, dendritic, and compact Morphologies, *ACS Appl. Mater. Interfaces*, 2020, **12**(13), 15885–15892.

64 Y. Nie, C. Liang, K. Zhang, R. Zhao, S. M. Eichfeld, P. R. Cha, L. Colombo, J. A. Robinson, R. M. Wallace and K. Cho, First-principles kinetic Monte Carlo study on the growth patterns of WSe_2 monolayer, *2D Mater.*, 2016, **3**(2), 25029.
65 M. Suleman, S. Lee, M. Kim, V. H. Nguyen, M. Riaz, N. Nasir, S. Kumar, H. M. Park, J. Jung and Y. Seo, NaCl-Assisted temperature-dependent controllable growth of large-area MoS_2 crystals using confined-space CVD, *ACS Omega*, 2022, **7**(34), 30074–30086.
66 S. Zhou, L. Gan, D. Wang, H. Li and T. Zhai, Space-confined vapor deposition synthesis of two dimensional materials, *Nano Res.*, 2018, **11**, 2909–2931.